Efficient Hydrogen Production from Formic Acid Using a Benzothiazole-based Ru(II)-PN^3 Pincer Complex

Student

Raad Alqahtany [Raad.alqahtany@kaust.edu.sa]

Mentor

Suman Dhara [Suman.dhara@kaust.edu.sa]

Indranil Dutta [Indranil.dutta@kaust.edu.sa]

Supervisor

Kuo-Wei Huang [kuowei.Huang@kaust.edu.sa]

Abstract

Among several liquid organic hydrogen carriers, formic acid (FA) is a potential option due to its desirable properties, which allow for easy storage and transportation. To generate hydrogen on demand from FA, Ruthenium has become one of the most widely employed metal centers for homogeneous organometallic catalysts. Rational ligand design, particularly the development of pincer ligands, has enabled improved metal-ligand cooperativity and enhanced catalytic performance under milder conditions. Herein, we report a new class of PN^3 pincer ligand incorporating a benzothiazole backbone and its Ruthenium complex [Ru(PN^3)(CO)(H)(Cl)]. The pincer complex was characterized by ^{1}H NMR, ^{31}P NMR, ^{13}C NMR and single-crystal X-ray crystallography. Further, the conditions of catalysis have been optimized by altering the solvent, base, acid-amine ratio (AAR), and catalyst amount. From this, it was determined that the optimal reaction conditions are as follows: DMSO as the solvent, triethylamine as the base with 3:1 AAR, and 5 µmol catalyst loading. After optimization, our catalytic system has achieved a TOF of 5292 h^{-1}.

Contents

Contents *2*

1 Introduction *3*

2 Methodology *6*

2.1 Materials 6

2.2 Physical Measurements 6

2.3 Synthesis 6

2.3.1 Ligand Synthesis 6

2.3.2 Complex Synthesis 6

2.4 General Procedure for Dehydrogenation of FA 7

3 Results and Discussion *7*

3.1 Synthesis and Characterization 7

3.2 FA Dehydrogenation 10

3.3 Mechanism 11

4 Conclusion *12*

5 Future Work *12*

References *13*

Appendix *15*

1 Introduction

The continued development of industrial, technological and economic sectors has driven the increase in global energy demand.[1] Meanwhile, as fossil fuels remain the world's primary energy source (Figure 1A), their continued combustion has led to rising atmospheric carbon dioxide (CO_2) concentrations (Figure 1B), contributing to global warming and its associated environmental impacts.[2] This highlights the urgent need to transition to clean, sustainable energy alternatives. Renewable energy sources such as solar and wind power can be considered viable alternatives to fossil fuels.[3] Nevertheless, their large-scale integration into modern energy systems remains constrained by resource intermittency, geographical constraints and energy storage and transportation challenges.[4]

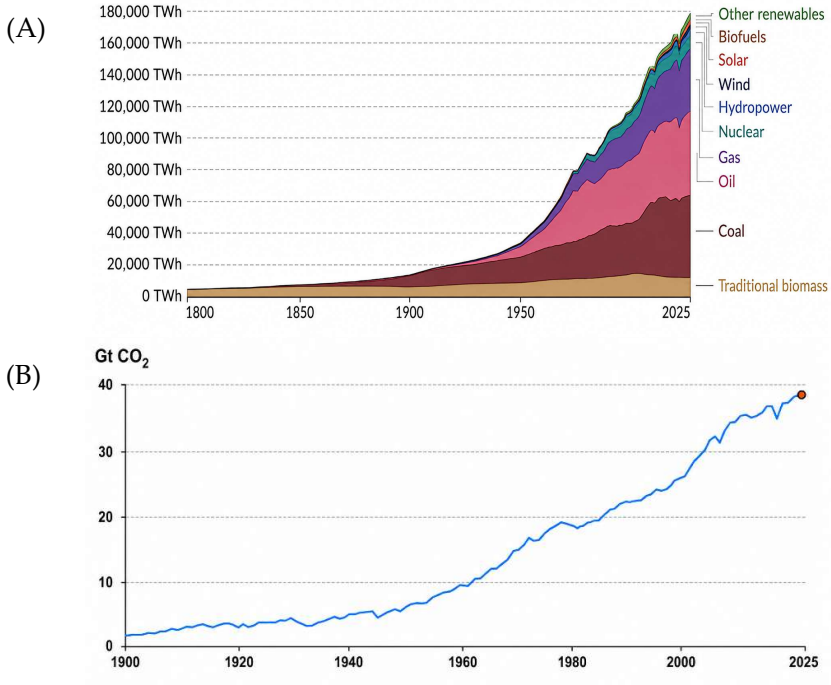


Figure 1. (A) Historical development of global primary energy consumption[5]; (B) Global CO_2 emissions from energy and industrial activities.[6]

In this regard, Hydrogen (H_2) has therefore attracted considerable attention as a promising clean energy carrier for the transition toward sustainable energy.[7] Unlike fossil fuels, its utilization via fuel cells produces only water as a by-product while offering the highest gravimetric energy density of any known combustible fuel (33.3 kWh kg^{-1}), making it an attractive alternative to conventional fossil fuels.[8] However, despite these advantages, the widespread implementation of hydrogen energy systems remains challenging as it depends significantly on the development of efficient technologies for storage and transportation. The storage of H_2 specifically remains a major challenge due to its low volumetric density, requiring highly pressurized cylinders or cryogenic liquid tanks. These conventional methods are associated with considerable energy losses resulting from hydrogen compression, liquefaction and fugitive hydrogen emissions, which may also contribute to global warming.[9]

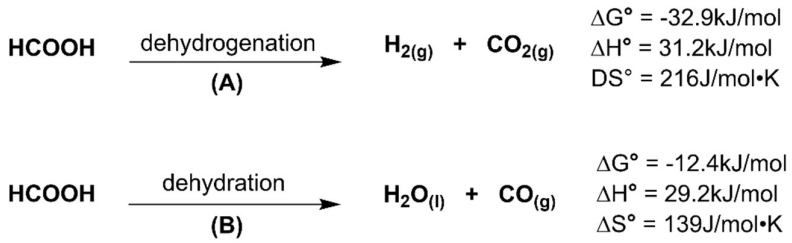
Consequently, liquid organic hydrogen carriers (LOHCs) offer a solution for hydrogen storage, as they chemically bind and release hydrogen through reversible hydrogenation and dehydrogenation reactions, enabling safe storage and transportation under ambient conditions.[10]

Their liquid nature also facilitates integration with the existing fuel distribution infrastructure while allowing repeated use through reversible chemical cycles. A wide range of LOHCs has been investigated for hydrogen storage applications, as summarized in Table 1. Among them, FA demonstrates the most significant efficiency as LOHC. FA has high volumetric hydrogen storage capacity (53 g H_2 L^{-1}) while it is nontoxic and non-flammable under ambient conditions and has lowest dehydrogenation temperature.[11]

Table 1. Comparison of selected liquid hydrogen carriers.[12]

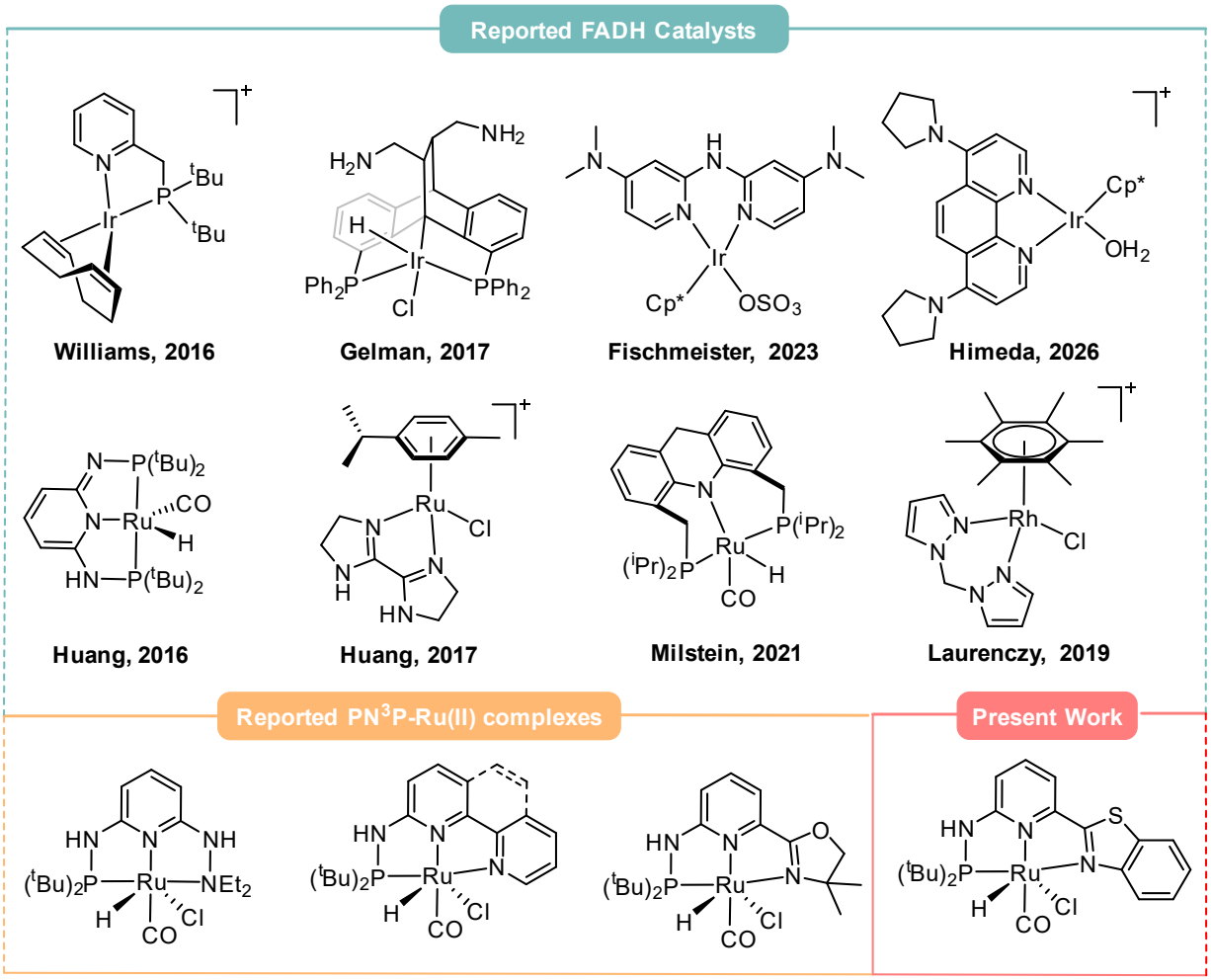
Properties	H_2	MCH	NH_3	HCOOH (85%)
Phase	Liquid	Liquid	Liquid	Liquid
Boiling Point (°C)	–253	101	-33	100.8
Density (kg m^{-3})	70.8	770	680	1220
Volumetric H_2 content (Kg_{H2} m^{-3})	70.8	47.1	120	53
Gravimetric H_2 content (wt%)	100	6.1	17.65	4.38
H_2 release process	Evaporation	Dehydrogenation (350°C)	Cracking (>425°C)	Dehydrogenation (<100°C)
Nature	Highly flammable	Toxic	Toxic	Low-flammability/low-toxicity

FA decomposition involves two competing parallel pathways (Scheme 1); one pathway is formic acid dehydrogenation (FADH), which yields carbon dioxide and hydrogen ($HCOOH \rightarrow CO_2 + H_2$).[12] Then, the generated hydrogen can be utilized for green hydrogen fuel, while CO_2 can be captured and hydrogenated back to FA through carbon dioxide hydrogenation (CDH). In contrast, the other pathway is FA dehydration, which yields water and carbon monoxide ($HCOOH \rightarrow H_2O + CO$). Unlike FADH, this pathway does not produce hydrogen; water can destabilize the fuel cell while the generated CO is highly toxic and can poison fuel-cell catalysts, making it undesirable for hydrogen energy applications.[11,12] Hence, it is important to develop catalysts that exhibit high selectivity toward the FADH pathway.



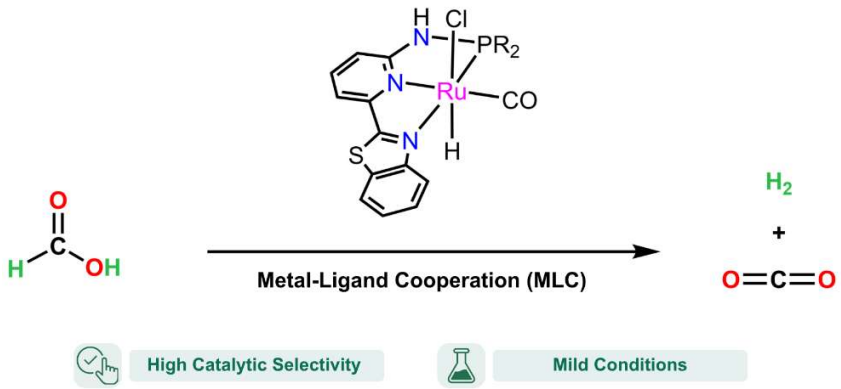
Scheme 1. FA decomposition pathways (A) dehydrogenation. (B) dehydration.

To this end, homogeneous organometallic catalysts based on transition and noble metals have been investigated for selective FADH (Scheme 2).[13-17] Ruthenium has become one of the most widely employed metal centers for homogeneous organometallic catalysts.[18-20] The catalytic performance of ruthenium complexes is strongly governed by the ligand framework, where pincer ligands provide a robust coordination environment capable of promoting metal-ligand cooperation (MLC).[21] This cooperative behavior enables the metal center and the ligand to participate in substrate activation, enhancing catalytic activity and selectivity.



Scheme 2. Reported 4d/5d-metal based FADH catalysts along with some PN^3(P) ligand-incorporated Ru(II) pincer complexes.

Hence, the continued development of ruthenium pincer complexes with new ligand architectures remains important for further improving catalytic efficiency and stability.[22-23] Herein, a benzothiazole-based Ru(II)-PN^3 pincer complex catalyst (Scheme 3) was synthesized and characterized for selective FADH.



Scheme 3. Ru(II) pincer complex-catalyzed FA dehydrogenation.

2 Methodology

2.1 Materials

All chemicals and solvents were obtained from commercial suppliers and used as received without further purification unless otherwise stated. Toluene, tetrahydrofuran (THF), dimethyl sulfoxide (DMSO), chloroform ($CHCl_3$), ethyl acetate, and petroleum ether were used as solvents. Silica gel and TLC plates were obtained commercially. All materials were used under the fume hood unless otherwise stated.

2.2 Physical Measurements

$^{1}H/^{13}C/^{31}P$ NMR spectra were recorded on a Bruker Avance III 400 MHz or a Bruker Avance III 500 MHz spectrometer. Electrospray mass spectrometry (ESI-MS) was performed on a Bruker Maxis Impact (282 001.0008) spectrometer. IR spectrum of solid samples (in KBr pellets) in the range 400-4000 cm^{-1} was recorded on a Perkin-Elmer spectrophotometer. GC analysis of the evolved gases was performed using an Agilent 7890A GC system.

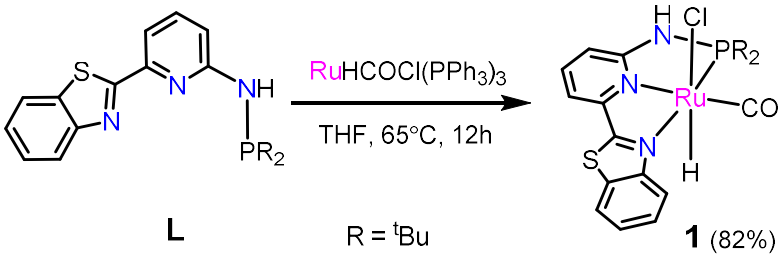
2.3 Synthesis

2.3.1 Ligand Synthesis

The desired ligand was synthesized according to the reported procedure of an analogous ligand.[22]

2.3.2 Complex Synthesis

In a 25 mL pressure vessel equipped with a magnetic stirring bar were placed the ligand (100 mg, 0.27 mmol), $[Ru(PPh_3)_3HCl(CO)]$ (256 mg, 0.27 mmol), and 10 mL of dry THF were placed under an argon glovebox. The flask was sealed and heated to 65°C overnight (Scheme 4). Then the reaction mixture was cooled to room temperature, and red precipitates were formed. The solid was filtered, washed with pentane (5.0 mL × 3), and dried in vacuo to afford pure complex (118 mg, 82%). ^{1}H NMR (400 MHz, $(CD_3)_2SO$): δ 8.75 (s, 1H), 8.33 (d, J = 8.1 Hz, 1H), 8.27 (d, J = 8.3 Hz, 1H), 7.82 (dt, J = 14.7, 7.8 Hz, 2H), 7.72 (d, J = 7.4 Hz, 1H), 7.67 (t, J = 7.7 Hz, 1H), 7.19 (d, J = 8.4 Hz, 1H), 1.46 (d, J = 14.4 Hz, 9H), 1.28 (d, J = 14.3 Hz, 9H), -16.05 (d, $^{2}J_{PH}$ = 26.2 Hz, 1H, Ru-H); 13C NMR (101 MHz, $(CD_3)_2SO$): δ 207.95, 207.80, 164.78, 160.66, 150.34, 148.63, 138.79, 133.00, 127.99, 127.31, 123.60, 123.05, 113.95, 110.76, 29.62, 29.56, 28.74, 28.70; ^{31}P NMR (162 MHz, $(CD_3)_2SO$): δ 159.40. MS (ESI+, CH_3CN): m/z for [**1**–Cl]$^{+}$ calculated 502.0655; found 502.0651. IR (KBr, cm^{-1}): 1920 [ν(C≡O)].



Scheme 4. Synthetic route for the preparation of the Ru(II)-PN^3 pincer complex.

2.4 General Procedure for Dehydrogenation of FA

FA dehydrogenation experiments were carried out in a 25 mL two-necked round flask equipped with a reflux condenser and a magnetic stirrer at the mentioned temperature. FA (26 mmol) was taken in a two-necked round flask in DMSO (5 mL) and heated at the desired temperature. Next, the catalyst was added to the reaction solution. The reaction mixture was stirred continuously at the desired temperature. The volume of gas evolved during the reaction was measured using an ADM G6691A flowmeter simultaneously (Figure 2). The data were collected every 2 s to the computer by LabVIEW.

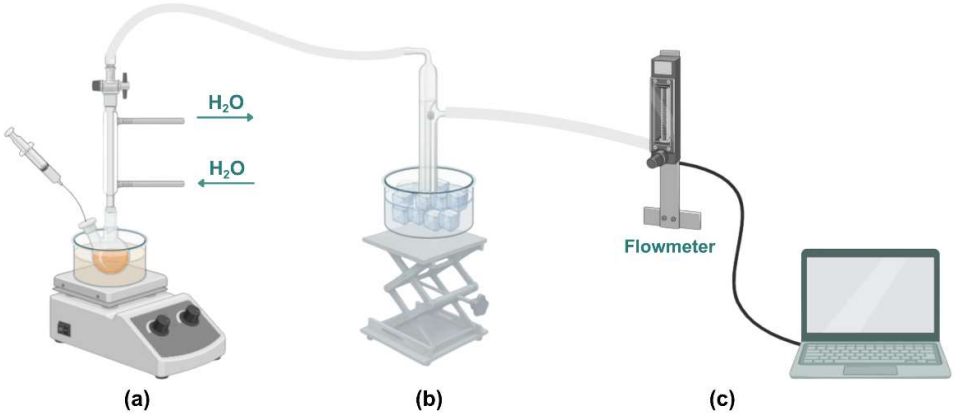


Figure 2. General work setup for FADH. (a) Reaction flask containing the catalyst solution; FA and base were injected to initiate the reaction. (b) Solvent trap. (c) Flowmeter for continuous recording of the gas volume.

3 Results and Discussion

3.1 Synthesis and Characterization

The mononuclear ruthenium complex **1** was obtained by the reaction of **L** with the corresponding metal precursor $Ru^{II}(H)(Cl)(CO)(PPh_3)_3$ in a heated tetrahydrofuran medium under an argon atmosphere. The formation of complex **1** was authenticated by electrospray mass spectrometry/infrared (IR)/^{1}H/^{31}P NMR, as well as by single-crystal X-ray diffraction. The single-crystal X-ray structure of the complex is shown in Figure 3. The asymmetric unit of the crystal consisted of an equatorially coordinated PN^3 pincer ligand (**L**), carbon monoxide ligand opposite the central pyridine of the ligand moiety. The remaining two axial positions of the central octahedral ruthenium atom were occupied by a hydride and a chloride atom. Diamagnetic complex **1** exhibited a well-defined calculated number of proton resonance peaks within the chemical shift range from 9 ppm to -17 ppm (Figure 4). The aromatic protons of the pyridine as well as the benzothiazole moiety appeared between 7 and 8.5 ppm, whereas the aliphatic protons of the tBu group resonated in the range of 1.3 to 1.5 ppm. The NH and Ru-H peaks are located at 8.73 and -16.04 ppm as a singlet and doublet, respectively. ^{13}C NMR spectrum of the complex displayed the calculated number of peaks, including the carbonyl carbon peak at 207.8 ppm (Figure 5). ^{31}P NMR profile demonstrated a peak at 159.40 as a doublet due to the coupling with Ru-H (Figure 6). The HRMS spectrum peak of **1** at 502.0651 m/Z corresponded to the $[1–Cl]^+$ species (Figure 7A). Furthermore, the Fourier transform infrared (FTIR) spectrum revealed a sharp CO peak at 1920 cm^{-1}, consistent with the CO bond stretching frequency of Ru-CO along with νRu-H at 2035 cm^{-1} (Figure 7B).

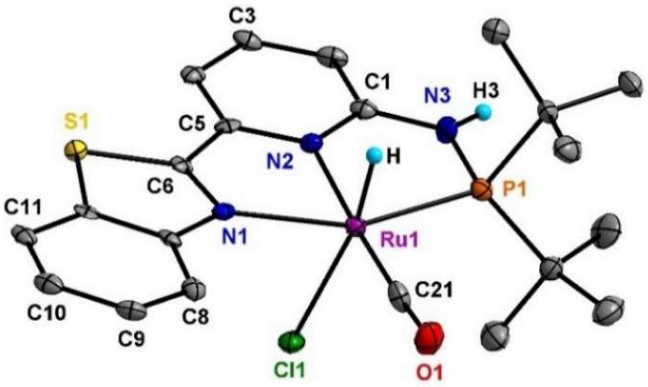


Figure 3. Single-crystal X-ray structure of **1**. Thermal ellipsoids are drawn at 35% probability level. Solvent molecules and most H atoms are omitted for clarity.

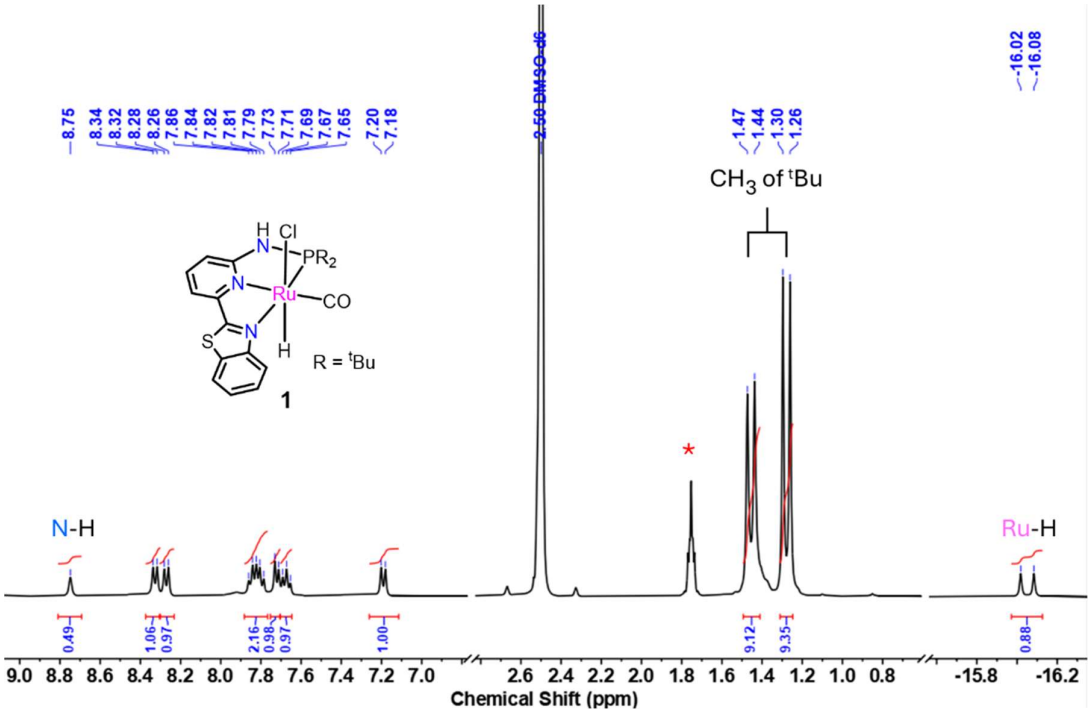


Figure 4. ^{1}H NMR spectrum of **1** in $(CD_3)_2SO$. * indicates THF molecules.

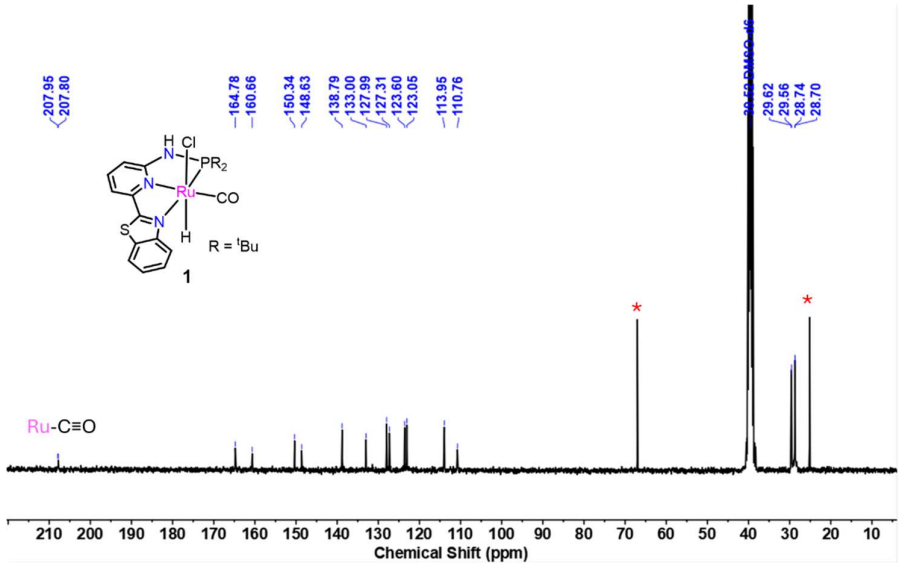


Figure 5. ^{13}C NMR spectrum of **1** in $(CD_3)_2SO$. * indicates THF molecules.

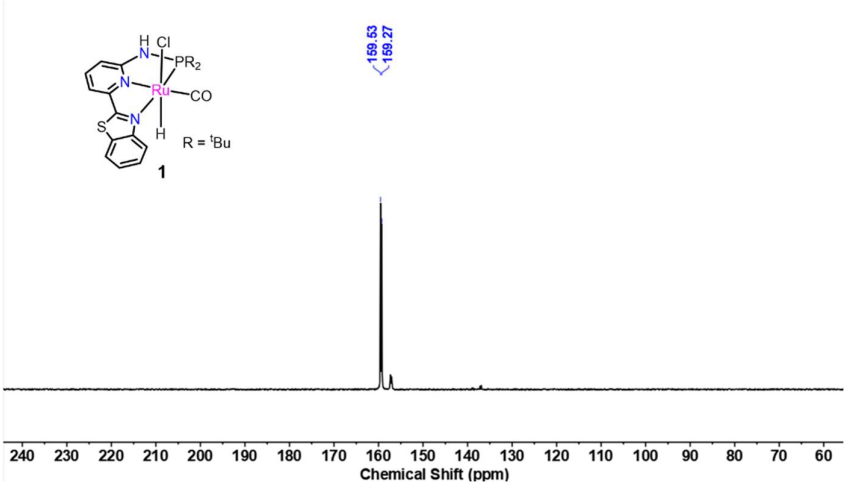


Figure 6. ^{31}P NMR spectrum of **1** in $(CD_3)_2SO$.

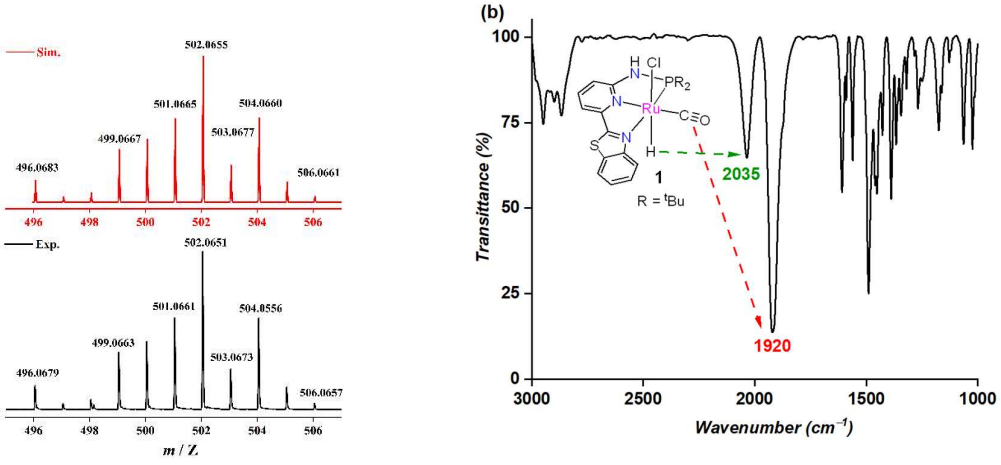


Figure 7. (a) ESI-MS (+) spectrum of **1** in CH_3CN; (b) FT-IR spectrum of **1**.

3.2 FA Dehydrogenation

The initial study was conducted in DMSO at 80°C using complex **1** with triethylamine (NEt_3) as the base and an acid-to-base molar ratio (AAR) of 3, yielding a TOF of 1740 h-1 (Table 2, entry 1). Lowering the reaction temperature to 70°C reduces catalyst reactivity, whereas at 90°C, catalyst performance increases (Table 2, entry 3). Further increment in temperature to 100°C was avoided as it reached the FA boiling point. The effect of catalyst loading was evaluated by varying the catalyst amount from 2 to 5 µmol, with the highest reactivity observed at 5 µmol (5292 h^{-1}; Figure 9). The base was found to be essential for the reaction, as no gas evolution was observed in the absence of NEt_3 (entry 10, Table1). Optimization of the base loading further demonstrated that the highest reactivity was achieved using 3 equivalents of acid (FA) with 1 equivalent of base NEt_3 (entry 3, Table 1). Excessive use of base harmed the reaction rate (entries 7-8, Table 1). Besides NEt_3, sodium formate (HCOONa) was also evaluated as a base, resulting in only trace gas evolution under the reaction conditions (entry 9, Table 1).

Table 2. Ru(II)-catalyzed hydrogen production from FA

Entry	base	T [°C]	Cat. [µmol]	AAR	H_2+CO_2 (ml)	TOF [h^{-1}]
1	NEt_3	80	5	3	1321	1740
2	NEt_3	70	5	3	458	500
3	NEt_3	90	5	3	1338	5292
4	NEt_3	90	4	3	1346	4956
5	NEt_3	90	3	3	1290	4430
6	NEt_3	90	2	3	1140	3821
7	NEt_3	90	5	1	1320	4928
8	NEt_3	90	5	1/3	848	1162
9	HCO_2Na	90	5	3	trace	---
10	NEt_3	90	0	3	---	----

TOF was determined from the gas production measured during the first 10 min of the reaction (details of the calculation in the appendixes).

Finally, the role of solvent was also evaluated. Insolubility of complex **1** in aqueous medium caused no gas evolution in water. Furthermore, non-polar solvents such as toluene were ineffective, suggesting that polar reaction intermediates may be involved in the catalytic process (Table 3).

Table 3. Role of solvent on catalyst performance

Entry	Solvent	H_2+CO_2 (ml)	TOF [h^{-1}]
1	DMSO	1338	5292
2	H_2O	---	---
3	Toluene	---	---

1 (5 µmol), 1 ml FA (26mmol), NEt_3 (8.67 mmol), solvent (5mL), 90°C

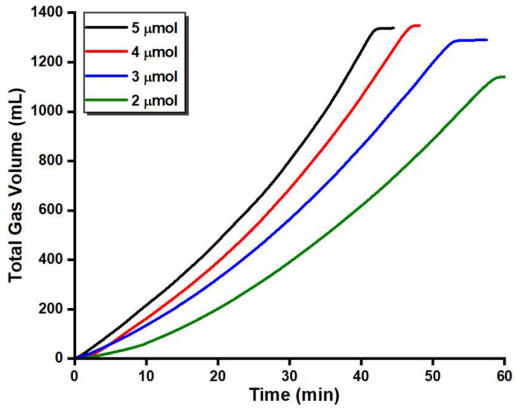


Figure 9. Total Gas (H_2+CO_2) evolution over time.

The FA dehydrogenation selectivity was further confirmed by gas chromatographic analysis of the evolved gas (Figure 10). The analysis revealed the formation of H_2 and CO_2, with no detectable CO, demonstrating the excellent selectivity of the catalytic system for the dehydrogenation pathway over dehydration.

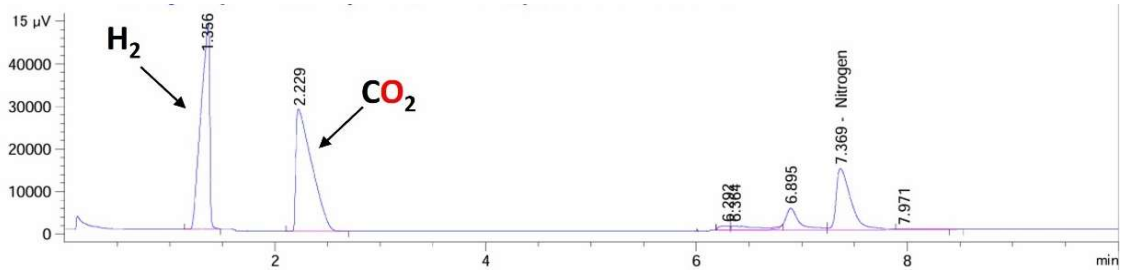
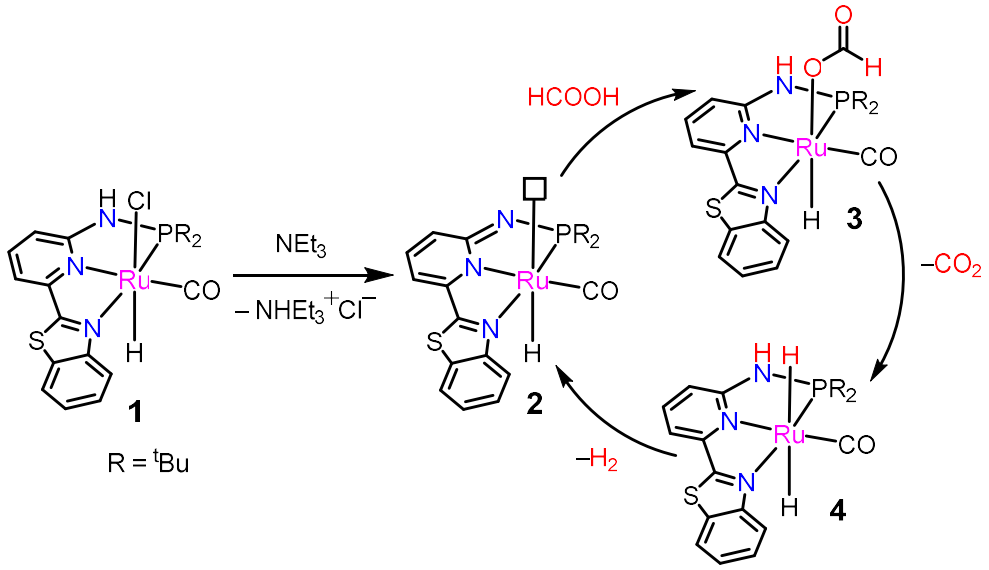


Figure 10. Composition analysis of the evolved gas mixture by GC-TCD analysis.

3.3 Mechanism

Based on literature and chemical intuition, the following reaction mechanism is proposed for the Ruthenium PN^3 pincer complex-catalyzed FADH process (Scheme 4). The aromatized complex **1** is first converted to its dearomatized version **2** in the presence of base, which abstracts the NH proton from the P^tBu_2 side arm. Complex **2** then reacts with FA and the reaction involves bifunctional activation of FA via the protonation of the imine bond and concomitant formation of metal-formate intermediate **3**. After that, intermediate **3** undergoes decarboxylation to form dihydridoruthenium species **4**, which finally regenerates complex **2** via the elimination of H_2.



Scheme 4. Proposed Mechanism for the catalyzed dehydrogenation of FA.

4 Conclusion

In this present work, we have synthesized a noble metal ruthenium-based pincer ligand complex having a benzothiazole-pyridine fused central core. The newly prepared complex was then characterized using various spectroscopic techniques like NMR/IR/Mass and its structural conformity was authenticated by single-crystal X-ray structures. Furthermore, the complex was tested for homogeneously catalyzed FADH reaction. Various parameters associated with the catalytic FADH process were optimized. Finally, with a catalyst loading as low as 5 μmol, we have achieved a TOF of 5292 h^{-1} under the reaction conditions of a 3:1 FA to NEt_3 ratio and 90°C reaction temperature. The pincer ligand used in this report plays an important role in activating the FA via the metal-ligand cooperation (MLC) concept, and it helped to maintain the metal oxidation state.

5 Future Work

Future studies will focus on evaluating the catalytic system under a broader range of reaction conditions, including the use of solvents such as acetonitrile and DMF for FADH. Detailed mechanistic investigations using various spectroscopic techniques, particularly NMR spectroscopy, will be undertaken to identify the intermediate and active species involved in the reaction. In addition, kinetic isotope effect (KIE) studies using deuterated FA will be performed to gain insights into the rate-determining step of the catalytic process. Furthermore, density functional theory (DFT) calculations of the reaction mechanism would be very useful

References

1. The International Energy Outlook **2023** *(IEO2023).* https://www.eia.gov/outlooks/ieo/
2. IEA (2026), Global Energy Review **2026**, IEA, Paris. https://www.iea.org/reports/global-energy-review-2026
3. Ang, T.-Z.; Salem, M.; Kamarol, M.; Das, H. S.; Nazari, M. A.; Prabaharan, N. A comprehensive study of renewable energy sources: Classifications, challenges and suggestions. *Energy Strategy Rev.* **2022**, *43*, 100939.
4. Foqha, T.; Refaat, S. S.; Mohammed, A.; Farrag, M.; Gamal, H. Renewable energy sources: Progress, challenges, and environmental benefits. *Renew. Sustain. Energy Rev.* **2026**, 240, 117167.
5. Global primary energy use by source: *Our World in Data* https://ourworldindata.org/grapher/global-primary-energy-by-source.
6. CO_2 emissions-Global Energy Review 2026 – Analysis. *IEA* https://www.iea.org/reports/global-energy-review-2026/co2-emissions.
7. Bhuiyan, M. M. H.; Siddique, Z. Hydrogen as an alternative fuel: A comprehensive review of challenges and opportunities in production, storage, and transportation. *Int. J. Hydrog. Energy* **2025**, *102*, 1026-1044.
8. Møller, K. T.; Jensen, T. R.; Akiba, E.; Li, H. Hydrogen - A sustainable energy carrier. *Prog. Nat. Sci. Mater. Int.* **2017**, *27*, 34-40.
9. Dutta, I.; Parsapur, R. K.; Chatterjee, S.; Hengne, A. M.; Tan, D.; Peramaiah, K.; Solling, T. I.; Nielsen, O. J.; Huang, K. -W. The Role of Fugitive Hydrogen Emissions in Selecting Hydrogen Carriers. *ACS Energy Lett.* **2023**, *8*, 3251-3257.
10. Reymond, A., Camilli, L., Marti, A., Araque, M. & Wojcieszak, R. Liquid Organic Hydrogen Carriers (LOHCs): Comprehensive Comparison and Future Outlook. *Energy Fuels* **40**, 3443–3468 (2025).
11. Eppinger, J.; Huang, K.-W. Formic Acid as a Hydrogen Energy Carrier. *ACS Energy Lett.* **2017**, *2*, 188-195.
12. Dutta, I.; Chatterjee, S.; Cheng, H.; Parsapur, R. K.; Liu, Z.; Li, Z.; Ye, E.; Kawanami, H.; Low, J. S. C.; Lai, Z.; Loh, X. J.; Huang, K. -W. Formic Acid to Power towards Low-Carbon Economy. *Adv. Energy Mater.* **2022**, *12*, 2103799.
13. Celaje, J. J. A.; Lu, Z.; Kedzie, E. A.; Terrile, N. J.; Lo, J. N.; Williams, T. J. A Prolific Catalyst for Dehydrogenation of Neat Formic Acid. *Nat. Commun.* **2016**, *7*, 11308.
14. Cohen, S.; Borin, V.; Schapiro, I.; Musa, S.; De-Botton, S.; Belkova, N. V.; Gelman, D. Ir(III)-PC(sp^3)P Bifunctional Catalysts for Production of H_2 by Dehydrogenation of Formic Acid: Experimental and Theoretical Study. *ACS Catal.* **2017**, *7*, 8139-8146.
15. Guo, L.; Li, Z.; Cordier, M.; Marchal, R.; Guennic, B. L.; Fischmeister, C. Noninnocent Ligands for Efficient Dehydrogenation of Aqueous and Neat Formic Acid under Base-Free Conditions. *ACS Catal.* **2023**, *13*, 13626-13637.
16. Maji, B.; Chandrasekaran, S.; Hirose, T.; Onishi, N.; Himeda, Y. Highly Robust Diamino-Substituted Phenanthroline-Based Iridium Catalysts for Dehydrogenation of Formic Acid in Water with Mechanistic Insights. *ACS Catal.* **2026**, *16*, 2450-2457.
17. Fink, C.; Laurenczy, G. A Precious Catalyst: Rhodium-Catalyzed Formic Acid Dehydrogenation in Water. *Eur. J. Inorg. Chem.* **2019**, 2381-2387.
18. Pan, Y.; Pan, C. -L.; Zhang, Y.; Li, H.; Min, S.; Guo, X.; Zheng, B.; Chen, H.; Anders, A.; Lai, Z.; Zheng, J.; Huang, H. -W. Selective Hydrogen Generation from Formic Acid with Well-Defined Complexes of Ruthenium and Phosphorus-Nitrogen PN^3-Pincer Ligand. *Chem. Asian J.* **2016**, *11*, 1357-1360.

19. Guan, C.; Zhang, D.; Pan, Y.; Iguchi, M.; Ajitha, M. J.; Hu, J.; Li, H.; Yao, C.; Huang, M. -H.; Min, S.; Zheng, J.; Himeda, Y.; Kawanami, H.; Huang, K. -W. Dehydrogenation of Formic Acid Catalyzed by a Ruthenium Complex with an N,N′-Diimine Ligand. *Inorg. Chem.* **2017**, *56*, 438-445.
20. Kar, S.; Rauch, M.; Leitus, G.; Ben-David, Y.; Milstein, D. Highly Efficient Additive-Free Dehydrogenation of Neat Formic Acid. *Nat. Catal.* **2021**, *4*, 193-201.
21. Li, H.; Gonçalves, T. P.; Lupp, D.; Huang, K. -W. PN^3(P)-Pincer Complexes: Cooperative Catalysis and Beyond. *ACS Catal.* **2019**, *9*, 1619-1629.
22. Chen, T.; Li, H.; Qu, S.; Zheng, B.; He, L.; Lai, Z.; Wang, Z. -X.; Huang, K. -W. Hydrogenation of Esters Catalyzed by Ruthenium PN^3-Pincer Complexes Containing an Aminophosphine Arm. *Organometallics* **2014**, *33*, 4152-4155.
23. Li, H.; Wang, Y.; Lai, Z.; Huang, K. -W. Selective Catalytic Hydrogenation of Arenols by a Well-Defined Complex of Ruthenium and Phosphorus-Nitrogen PN^3-Pincer Ligand Containing a Phenanthroline Backbone. *ACS Catal.* **2017**, *7*, 4446-4450.

Appendix

TON and TOF Calculations

To calculate TON and TOF, the sum of the H_2 and CO_2 volumes is taken as the total volume. Total volume was calculated as the product between the number of moles and the molar volume of the species.

$$\mathrm{V}_{H_2} + \mathrm{V}_{CO_2} = \mathrm{V}$$

$$\mathrm{n}_{H_2}\mathrm{V}_{m,H_2} + \mathrm{n}_{CO_2}\mathrm{V}_{m,CO_2} = \mathrm{V}$$

$$n(\mathrm{V}_{m,H_2} + \mathrm{V}_{m,CO_2}) = \mathrm{V}$$

$$n = \frac{\mathrm{V}}{(\mathrm{V}_{m,H_2} + \mathrm{V}_{m,CO_2})}$$

$TON = \frac{\mathrm{n}}{n_{cat}}$ where n_{cat} is the number of moles of the catalyst

$TOF = \frac{\mathrm{TON}}{T}$ where T is time in hours (h)

In Table 2, the TOF is calculated at the initial 10 min (T = 0.1667 h); therefore, the TOF will be calculated as follows

$$TOF_{10\ min} = \frac{\mathrm{TON}_{10\ min}}{0.1667\ h}$$

To calculate the molar volume for both H_2 and CO_2, the following equations were used:

$$\mathrm{V}_{m,H_2} = \frac{RT}{p} + b - \frac{a}{RT} = 24.48\ L\ mol^{-1}$$

Where:

$R = 8.31447\ m^3 Pa\ mol^{-1} K^{-1}$

$T = 298.15\ K$

$p = 101325\ Pa$

$b = 26.7 \times 10^{-6}\ m^3 mol^{-1}$

$a = 24.9 \times 10^{-3}\ Pa\ m^6 mol^{-2}$

$$\mathrm{V}_{m,CO_2} = \frac{RT}{p} + b - \frac{a}{RT} = 24.36\ L\ mol^{-1}$$

Where:

$R = 8.31447\ m^3 Pa\ mol^{-1} K^{-1}$

$T = 298.15\ K$

$p = 101325\ Pa$

$b = 42.7 \times 10^{-6}\ m^3 mol^{-1}$

$a = 36.5 \times 10^{-2}\ Pa\ m^6 mol^{-2}$

$\mathrm{n}_{H_2} = \mathrm{n}_{CO_2} = \mathrm{n}$